Chapter 16. Reconstruction and Analysis of Intravascular Ultrasound Sequences

Francesco Ciompi [a,b,*], Carlo Gatta [b], Oriol Pujol [a,b], Oriol Rodríguez-Leor [c], Josepa Mauri Ferré [c], Petia Radeva [a,b]

[a]Universitat de Barcelona, Gran Via de les Corts Catalanes 585, 08007 Barcelona (Spain)
[b]Computer Vision Center, Edifici O, Campus UAB, 08193 Bellaterra, Barcelona (Spain)
[c]Hospital Universitari Germans Trias i Pujol, Carretera de Canyet s/n, 08916 Badalona (Spain)
[*]E-mail: fciompi@maia.ub.es

Abstract: Atherosclerotic plaque has been identified as one of the most important causes of sudden cardiac failure in patients with no history of heart disease. IntraVascular UltraSound (IVUS) represents a unique technique to study, determine and quantify plaque composition and thus allows to develop automatic diagnostic and prediction techniques for coronary diagnosis and therapy. However, one of the main problems of image-based studies is its dependence on image brightness and data miss-registration due to the dynamic system composed by the catheter and the vessel. Hence, the high dependence of the automatic analysis on the gain setting of IVUS console and its transmit power as well as vessel motion make impossible direct analysis, comparison and follow up of IVUS studies. To this purpose, a complete framework for data analysis should be considered focusing on: *a*) modeling the image acquisition and formation process, *b*) developing techniques for removing data acquisition artifacts due to the nature of ultrasound reflectance and motion of coronary vessels, *c*) developing sophisticated tools for extracting features from radio-frequency and images, and *d*) designing robust methods to discover and classify different categories of tissue structures. In this chapter, we overview different methodologies to approach the afore-mentioned problems and outline possible computer-assisted applications in the clinical practice.

Key words: Intravascular Ultrasound, Ultrasonography, Tissue Characterization, Swinging Effect, Rigid Registration, Radio Frequency Analysis

1. Introduction: Clinical Motivation

Coronary heart disease is a leading cause of death in the most developed countries, representing in Europe the 21% of mortality cause that accounts for 2 millions of lives (Fig.**1**). Atherosclerosis is the underlying mechanism for unstable angina, myocardial infarction and sudden cardiac death. Atherosclerotic plaque formation results from the proliferation, then destruction of intimal fibrosis tissue, resulting in the formation of an atheroma, i.e. a thickening of the *intimal-medial* segments and an overall thickening of the vessel wall (Fig.**2**). Plaques might be circumferential and occupy the entire perimeter of a vessel or be eccentric and occupy only a portion of the vessel wall. Luminal narrowing of the arteries is the main cause of the chronic ischemic manifestation of coronary heart disease, whereas superimpositions of thrombi over the plaques lead to acute coronary syndromes. Myocardial infarction occurs when the atheromatous process prevents blood flow through the coronary artery [1].

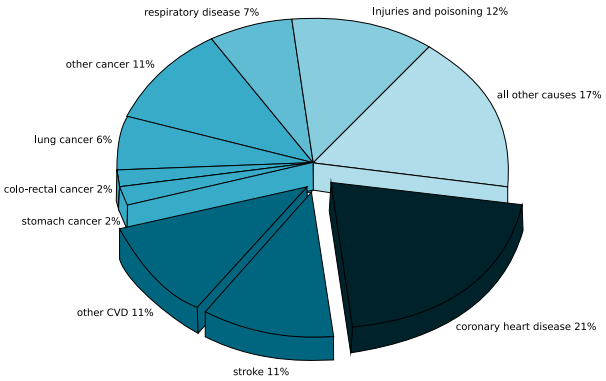

Figure 1: Deaths by cause, men, latest available year, Europe (from *European Cardiovascular Disease Statistics 2008*). Cardiovascular disease, stroke and coronary heart disease globally represent the 43% of death cause

Vulnerable plaques are atherosclerotic plaques prone to disruption and/or thrombosis. The exact nature of the vulnerable plaque is not yet well understood. The histology of atherosclerotic plaque is generally comprised of a mixture of layer upon layer of cholesterol debris, calcium, and fibrous tissue. Recent studies suggest that the vulnerable plaque could be determined as a mixture of known different tissue types. In this scenario, new diagnostic techniques for detecting vulnerable plaques become of extreme importance [2].

Angiography has always been considered as the *gold standard* imaging technique for detecting problematic arterial lesions and to guide therapy and percutaneous intervention for coronary disease. However, this diag-

Juan M. Górriz, Elmar W. Lang and Javier Ramírez (Eds)
All rights reserved - © 2011 Bentham Science Publishers Ltd.

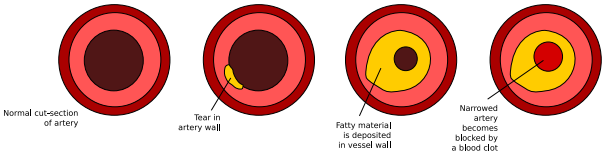

Figure 2: Atherosclerotic plaque formation. From the initial health condition (1), through the plaque formation (2), growth (3) and finally, the occlusion of the vessel with the formation of a blood clot (4) blocking the normal blood flow

nostic technique does not provide insight into the disease state within the artery, and often fails to detect those lesions prone to thrombosis.

In the last 10 years, Intravascular Ultrasound (IVUS) has evolved as a valuable adjunct to angiography. Whereas angiography depicts in fact only a 2D silhouette of the lumen, ultrasound allows precise tomographic visualization and measurement of lumen area and plaque size. This view is usually called *short-axis* view. It allows then the visualization of the full circumference of the vessel wall (Fig.**3**), thus showing the tissue distribution and, to some extent, composition. Hence, despite the independent value of IVUS, this technique should be considered supplemental to angiography, not a comprehensive alternative [3, 4].

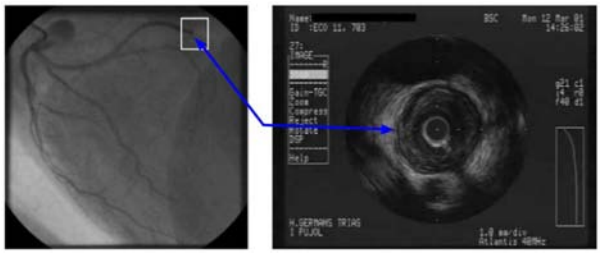

Figure 3: A coronary artery image by angiography (left) of the overall vessel morphology and corresponding IVUS image (right). While angiography allows to observe the 2D vessel morphology when the contrast agent is injected, the IVUS shows the inner morphological structure and content of the vessel

Plaque composition in ultrasound is usually characterized by the intensity of the signals as soft (gray) echoes, very high intensity (bright) reflectors that create distal shadowing, and echoes of intermediate intensity, features that correspond to tissue, calcification, and fibrosis, respectively (Fig.**5**). In addition, echolucent or signal free zones have been found to represent lipid accumulations. For these reasons, IVUS results to be a suitable technique for the assessment of atherosclerotic plaque in coronary artery analysis. In particular, it is appropriate in the study of the vulnerable plaque.

Due to the acquisition nature of the ultrasonic images by means of a pullback of the catheter a sequence of images is obtained. If the pullback is motorized with constant speed a notion of distance can be inferred from the

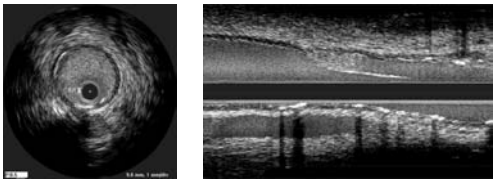

(*a*) (*b*)

Figure 4: (a) Standard *radial artery* cross-section view of an IVUS image and (b) corresponding longitudinal sequence (pullback). The longitudinal view is obtained by considering the graylevel values at a certain angle of the cross-sectional image during the whole sequence

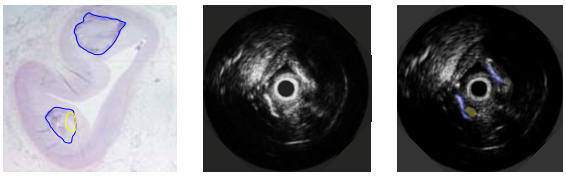

(*a*) (*b*) (*c*)

Figure 5: (a) Example of histological analysis of a post-mortem coronary artery cut and (b) corresponding IVUS image with (c) labeled plaques. In blue the *calcified* plaque and in yellow the *lipidic* plaque.

longitudinal view of the stack of images. The extension of the disease and the vessel morphology can be globally observed by this view. It allows in fact to detect diseased segments, positive or negative remodeling of the artery as well as the position of bifurcations and their plaque involvement. Furthermore, it is possible to measure the length of the plaque and to observe the lumen morphology, extremely important informations in order to decide which is the optimal stent to use.

However, the longitudinal view is affected by severe motion artifacts due to heart cycle that hinder the right interpretation and measurement process.

Starting from the analysis of the ultrasound-based image formation process, the main goal of this chapter is to describe the Intravascular Ultrasound image clinical modality, highlighting its properties and its usefulness in clinical case. Different approaches for the image reconstruction, filtering and processing are presented, in the context of coronary vessel modeling and plaque characterization techniques. The analysis motion artifacts due to motorized pullback acquisition is presented along with correction techniques yielding a more stable and reliable image sequence. Finally, by exploiting the differences in the US response provided by different tissue types, several IVUS based plaque characterization techniques are presented, mainly oriented to the automatic recognition of different plaque types.

2. ULTRASOUND TECHNOLOGY

Ultrasounds (US) are pressure waves with frequency f beyond the limit of human hearing ($f > 20$KHz), propagating in a medium.

In medicine, US are used in both diagnostic (*ultrasonography*) and therapeutic (*focused ultrasound surgery*) applications. In the first case, they are used to penetrate a medium and measure the reflection signature, which reveals details about the inner structure of the medium, while in the second case to supply focused energy to tissues.

In nature, each medium can be considered as formed by a large number of particles, normally quiet, that when perturbed by an US wave start to oscillate around their resting position. US in fact transfer mechanical energy through the medium they are traveling in, alternatively compressing and decompressing it [5].

Ultrasounds are generated by an US transducer able to both produce and receive pressure waves (Fig.**7**). When an US, propagating through a medium, finds an interface of two different tissues, it is in part reflected and returns towards the source with a reduced magnitude and a certain temporal delay: this phenomenon is called *echo* and it is common to each acoustic wave, not US only; for example, the echo of the voice into a well or in a big indoor environment. An ultrasound image is then created by processing the echoes returning to the US transducer from various depths of the body upon emission of an ultrasound pulse of a specific frequency.

In most of the ultrasonography application, the ultrasonic transducer is applied to the surface of the body, while in invasive application, like Intravascular Ultrasound, it is directly put into the artery. Four different modes of ultrasound are used in medical imaging [3]:

- **A-mode**, the simplest type of ultrasound: a single transducer scans a line through the body and the reflected echoes are studied as a function of depth. Therapeutic ultrasound aimed at a specific tumor or calculus is also A-mode, to allow for pinpoint accurate focus of the destructive wave energy;
- **B-mode**, where a linear array of transducers simultaneously scans a plane through the body that can be viewed as a two-dimensional image on screen;
- **M-mode**, where *M* stands for motion. It consists in a rapid sequence of B-mode scans whose images follow each other in sequence on screen; this modality enables doctors to see and measure range of motion, as the organ boundaries that produce reflections move relative to the probe;
- **Doppler-mode** Doppler is the effect of changing in frequency of a wave for an observer moving relative to the source of the wave and it is used to measure and to visualize blood flow.

In this chapter we focus our interest in the generation and the processing of A-lines, signals generated by A-mode ultrasound type, since they are the basis of the Intravascular Ultrasound technique.

2.1. Ultrasound image generation

Given its oscillatory nature, an US can be described by the following parameters: *wavelength* (λ), *frequency* (f) and *amplitude* (I) (Fig.**6**).

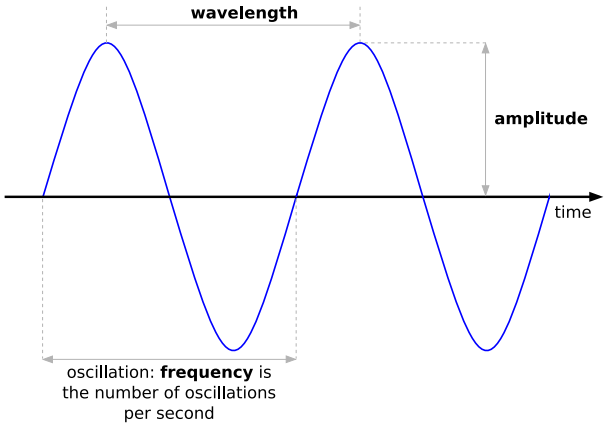

Figure 6: Example of a wave. The wavelength is the spatial distance between two maxima, the amplitude is the distance between the mean value (usually null) and the maximum. The period is the temporal delay between two consecutive maxima, while the frequency $f = 1/T$ is the number of oscillations per second

The velocity of the US propagating into the medium depends on the medium nature. If we consider the density ρ and the acoustic impedance ζ of the medium or, alternatively, the stiffness coefficient K, the velocity v of the propagating US is expressed as:

$$v = \frac{\zeta}{\rho} = \sqrt{\frac{K}{\rho}}, \tag{1}$$

from which we obtain

$$\zeta = \rho v. \tag{2}$$

Furthermore, the velocity v is related to the wave parameters as follows:

$$v = \lambda f. \tag{3}$$

In biological medium v can be assumed as constant; since human body mostly consists of water, usually we assume a value $v = 1,540 m/s$ for human tissues, while in bone it is around $v = 3,500 m/s$. Note that the low velocity of sound waves allow to measure their propagation time [5].

Ultrasounds are generated with *piezoelectric* transducer. Piezoelectric materials, like *quartz*, have the property of generating an electric voltage proportional to the pressure applied on them and vice-versa of changing

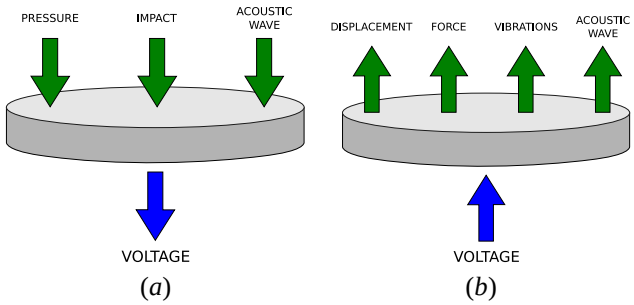

Figure 7: Schematized piezoelectric transducer. When a pressure, or even an acoustic (mechanical) wave impacts the piezoelectric probe, a voltage proportional to the amount of pressure is generated. Vice-versa, when the transducer is excited by an electrical signal, it deforms, thus generating pressure waves or vibrations

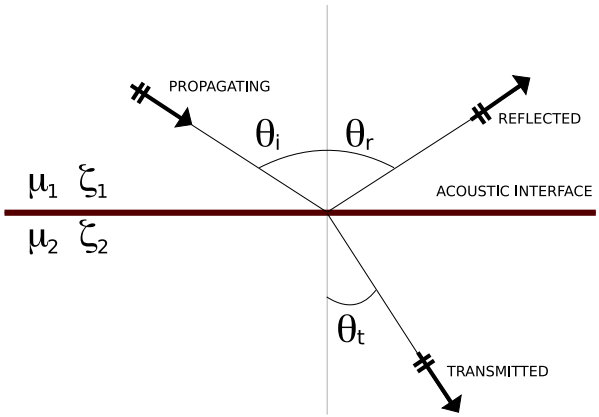

Figure 8: Acoustic interface between two generic tissue in contact: the propagating, reflected and transmitted wave are represented. The medium μ_1 is characterized by the acoustic impedance ζ_1 an the medium μ_2 by the impedance ζ_2

their dimension, thus generating pressure waves, when a voltage is applied. The piezoelectric transducer can be then used as US *generator*, when supplied by a voltage, or as US *receiver*, converting the mechanical excitement into an electric signal that can be processed (Fig.**7**).

All ultrasound techniques rely on the processing of *reflected sound waves* [5]. In the propagation of US into a medium, phenomena as *absorption*, *reflection* and *refraction* are observed. Let us consider two medium μ_1 and μ_2, characterized by their acoustic impedance ζ_1 and ζ_2, put in contact: a surface presenting a discontinuity of acoustic impedance arises (Fig.**8**). Let us consider an US wave, propagating through μ_1 (*propagating* wave) and reaching the discontinuity surface, with an angle θ_i. Consequently, a part of the wave propagates to μ_2 (*transmitted* wave) while a part of the wave keeps propagating through μ_1 (*reflected* wave) but with a different direction with respect to the propagating wave. The laws that regulate the relationship among the angles θ_i, θ_r and θ_t are:

$$sin\theta_i = sin\theta_r \tag{4}$$

that implies $\theta_i = \theta_r$ (*Reflection law*), and moreover:

$$\frac{sin\theta_i}{sin\theta_t} = \frac{v_i}{v_t} \tag{5}$$

known as Snell's law. From the previous equations, we can deduce that:

- if $v_1 = v_2$ there is no refraction and then the US keeps propagating without deviations ($\theta_i = \theta_t = 0$);
- if $\zeta_1 = \zeta_2$ there is no reflection and all the energy of the propagating wave is transmitted throught μ_2; in this case no echo signal is observed
- if $\zeta_1 \neq \zeta_2$ a part of the US energy is reflected ($\theta_i = \theta_r$) according to the reflection coefficient $0 \leq \Gamma \leq 1$, representing the amount of the reflected wave.

In the case of normal incidence ($\theta_i = \theta_t = 0$), Γ is:

$$\Gamma = \left(\frac{1 - \frac{\zeta_2}{\zeta_1}}{1 + \frac{\zeta_2}{\zeta_1}} \right)^2 . \tag{6}$$

If $\zeta_1 \gg \zeta_2$ or $\zeta_2 \gg \zeta_1$, as happens in the tissue/bone interface, all the incidence energy is reflected; in particular, if $\zeta_1 \gg \zeta_2$ a part of the wave is *scattered in all directions.*

Consequently, (*i*) if μ_2 has high echoreflectance (e.g. bone, calcified tissue) it avoids the transmission of the wave through the interface, thus generating a reflected wave with an amplitude similar to the propagating one, while (*ii*) if it has low echoreflectance, it will let transmit the wave, reflecting a small portion of it.

Given the relation among ζ (or ρ) and v, it becomes clear that an ultrasound scan does not visualize tissue structures directly but rather interfaces between tissues of different acoustic impedances: the greater the difference in impedance, the greater the reflection of the ultrasound wave and the smaller its transmission into deeper tissue.

The piezoelectric transducer receives then the reflected wave that presents different amplitude and a temporal delay (echo arrival time) respect to the generated pulse. By the attenuation the tissue type is recovered, while by the temporal delay the tissue position is established.

The intensity of the returning echoes also depends on the emitted frequency (see Eq.7). Attenuation increases with frequency and limits the penetration depth of the ultrasound pulse. The emitted intensity in fact decreases exponentially with distance from the source (the transducer) and is influenced by an attenuation coefficient α that varies with the type of tissue through which the beam travels in the human body (Fig.**9**). The average intensity in the body ranges from 0.3 to 0.6 decibels/MHz

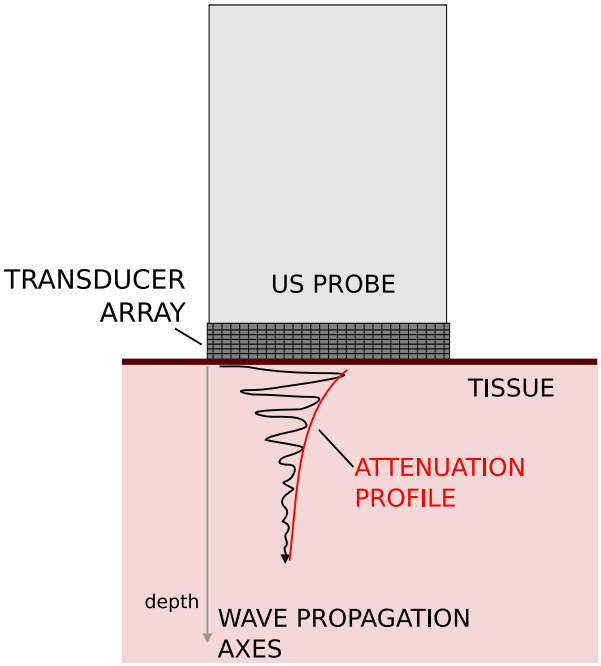

Figure 9: US wave attenuation phenomenon proportional to the tissue depth

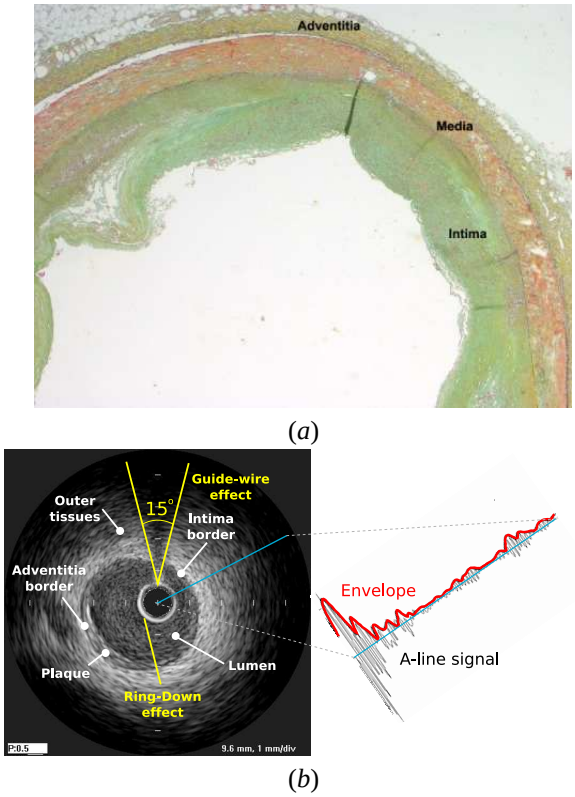

Figure 10: Morphology of a coronary artery. The intima-media-adventitia layers are indicated in (a) the histological image of a post-mortem artery, while corresponding layers are highlighted in (b) the IVUS image. An example of US signal generating the IVUS image is also represented, together with the envelope, proportional to the image gray level.

cm [5]. This phenomenon is usually compensated by a Time Gain Compensation function, as explained in next section.

3. INTRAVASCULAR ULTRASOUND IMAGING

Intravascular Ultrasound is a catheter-based imaging modality that provides an accurate luminal and transmural image of vascular structures [5]. Unlike angiography, which depicts a silhouette of the coronary lumen, IVUS in fact displays tomographic, cross-sectional perspective. This facilitates direct measurements of lumen dimensions, including minimum and maximum diameter and cross-sectional area as well as the characterization of atheroma size, plaque distribution and lesion composition (Fig.**10**) [6].

A typical IVUS image consists of three layers around the lumen: the *intima*, the *media* and the *adventitia*. The *intima* is normally a thin layer of endothelial cells: this layer substantially and often unevenly thickens in atherosclerosis. The *media* consists of multiple layers of smooth muscle cells arranged helically and circumferentially around the lumen of the artery; the normal medial thickness ranges from 125 to 350 μm although in the presence of plaque the medial thickness may be considerably thinner or even completely involuted and replaced by the plaque in several disease. Finally, the *adventitia* is the external layer, essentially composed by fibrous tissue, i.e. collagen and elastin [7].

Estimation of the vessel area is based on the measurements of the media-adventitia border, and plaque area is derived by subtracting lumen area from vessel area. Although invasive, the inside-out imaging of the arterial wall is extremely important in coronary interventions where there is limited access to the site of plaque deposition [8].

3.1. IVUS DATA ACQUISITION SYSTEMS

Images in IVUS are acquired by means of high-frequency, single-use probes based on various mechanical and electronic phased-array systems [5]. The probes are inserted into the vessel by a catheter with a diameter of 0.96 to 1.17 mm (2.9F to 3.5F in size). Two technical approaches to transducer design have emerged in years: *mechanically rotated* imaging devices and a *multi-element electronic array* device [6].

In multiple-element IVUS catheters, an array of piezoelectric transducers is disposed around the probe (see Fig.**11**), and an internal electronic device synchronizes the US waves emission. The plane of imaging is perpendicular to the long axis of the catheter and provides a

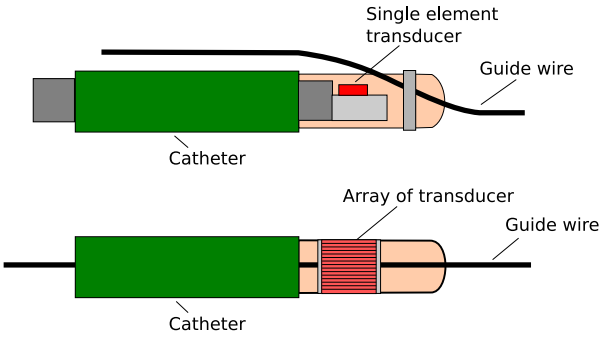

Figure 11: mechanical rotative (above) and phased array (below) IVUS catheters

full 360 degree image of the blood vessel. The used frequency for this type of catheters is in the range of 15-25 MHz. A problem of these imaging catheters, common to all high-frequency ultrasound devices to some extent, is the inability to image structure in the immediate vicinity of the transducer, i.e. in the"near field". Because the imaging crystal in a phased-array configuration is in almost direct contact with the structure being imaged, a bright circumferential artifact known as the "ring down" surrounds the catheter (Fig.**10**). The ring-down artifact can be electronically removed, but structures within the masked region will not be seen [9].

Mechanical transducers, the most frequently used type of IVUS catheters, consist in a single piezoelectric transducer, and the 360 degree view of the vessel is obtained by rotating the probe. Actually, two different configurations are available: (i) either the transducer itself or (ii) an acoustic mirror is rotated at the tip of the catheter using a flexible, high-torque cable that extends the length of the device. In the case in which the mirror is the rotating part, the transducer does not need to rotate and moreover can be put at a larger distance from the tissue. This fact partially reduces the ring-down effect and the poor resolution in the near-field [9]. In both rotating transducer and rotating mirror devices, ultrasound frequencies are between 12.5 and 40 MHz, although some experimental devices use up to 45 MHz [9]. In devices with a distally placed transducer and proximally rotating mirror, it is necessary for an electrical connecting wire to pass along the side of the imaging assembly. This wire produces an artifact that occupies approximately 15 degrees of the image cross-section (Fig. **10**). An interesting modification of the mechanical catheter design involves rotation of both the transducer and the mirror, eliminating any electrical wire artifact. Note that in the array-based IVUS catheter, the guide wire is placed in the center of the array and, therefore, it does not obstruct the ultrasound beam. In a single element system, the guide wire is on the side of the ultrasound element. The ultrasound beam, therefore, maybe reflected off of the guide wire and will result in bright echoes and shadow in the IVUS image.

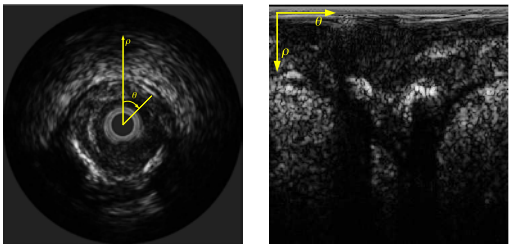

(*a*) (*b*)

Figure 12: (a) Standard cross-sectional IVUS image (in cartesian coordinates) and (b) its corresponding polar representation, obtained by processing the reflected US waves; ρ represents the depth in the tissue and θ the position (angle) in the rotation of the probe.

3.2. US IMAGE FORMATION

In both rotational and phased-array catheter, it is possible to reconstruct the 360 degree cross sectional representation of the inner vessel morphology. To form a transverse cross-sectional image of the vessel in real-time, the ultrasound beam is rotated at 30 revolutions per second leading to 30 images per second [8]. Each beam can be seen as a radius of the final circular IVUS image that shows the cross-section of the explored vessel (see Fig.**10**).

Given the number of position M assumed by the rotational catheter (or the number of transducer in the phased-array), during IVUS data acquisition, M A-lines are collected by the probe. The low speed of sound in human tissue (1,540 m/s) and the aim of achieving a high frame rate (real-time display) limit the number of ultrasound scan lines that can be used per image [5]. Each A-line can be sampled and N samples, quantized by using K-bit, are obtained. In this way, each IVUS frame can be stored and processed as an $M \times N$ matrix (Fig.**13**). The information contained in this matrix is actually related to the polar domain (r, θ) of the vessel morphology. The envelope of the A-line in fact corresponds to the amplitude of the reflected echo (Fig.**13**) at a certain depth.

TIME GAIN COMPENSATION (TGC). As the US propagating in the tissue is affected by an attenuation due to depth, first we apply TGC to data, defined as follows:

$$T(r) = 1 - e^{-\beta r}, \tag{7}$$

where $\beta = \ln 10^{\alpha f/20}$, α is the attenuation factor of the tissue measured in $dB/MHz \cdot cm$, f is the frequency of the transducer in MHz and r is the radial distance from the catheter in cm.

Different attenuation factors can be used for each tissue in order to be more precise in the vessel modelling. However, in practice this is not feasible since there is no

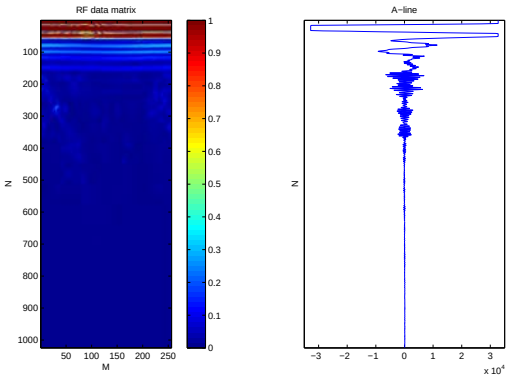

Figure 13: Raw RF data matrix (left) and a single A-line (rigth), actually representing one of the M columns of the data matrix. N is the number of samples and also represents the tissue depth. Note the exponential attenuation of the A-line while N increases

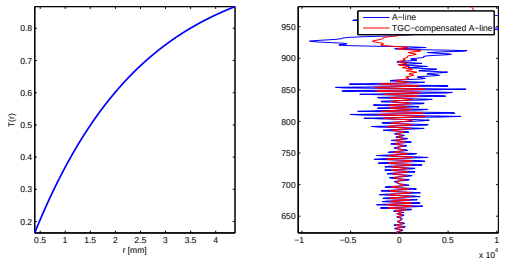

Figure 14: Example of Time-Gain-Compensation profile (left) used to compensate the attenuation phenomenon and (right) the TGC effect on the A-lin. Note that in the TGC-compensated profile, the signal range results more uniform

a priori information about the presence of specific tissues. Therefore, a weighted average of all possible factors is can be assumed ($\alpha = 0.1$ for example). Typical values for α for different parts of the human body are indicated in Table 1. The obtained profile is shown in Fig. **14**.

BAND PASS (BP) FILTER. Given the central frequency of the catheter f_0, we expect to find the main spectral information in a certain band centered in f_0. Data can be then filtered by a band-pass filter in order to reduce the noise effect and spurious harmonic components outside the band of interest. For this purpose, a Butterworth filter [10] is suitable, given that its frequency response is as flat as mathematically possible in the passband.

ENVELOPE. After filtering we need to recover the envelope of the signal to change from bipolar to unipolar signal, in order to achieve final conversion between 0 and 255. This is done by taking the absolute value of Hilbert transform of the signal (Fig. **10**).

NORMALIZATION. Data range is then changed between 0 and 1: this allows to work with homogeneous data ranges for all cases:

$$R_{norm} = \frac{R - R_{min}}{R_{max} - R_{min}}, \tag{8}$$

where R is the RF data matrix.

LOG TRANSFORMATION. This transformation maps a narrow range of low gray-level values in the input image into a wider range of output levels [11]:

$$R_{log} = \frac{\log(1 + (e^t - 1)R_{norm})}{t}. \tag{9}$$

GAMMA CORRECTION (optional). In order to expand the effective dynamic range of our digital images in terms of saturation, we can optionally apply the gamma correction using the *gamma value*, the gradient of the linear region on the *gamma value curve* [11]. A larger gamma results in a higher contrast image: $R_\gamma = R_{log}^\gamma$.

Finally, R_γ can be converted from polar to cartesian coordinates and the typical cross-sectional IVUS image of Fig. **10** is obtained. Hence, the radial component of R_γ is usually subsampled by a factor of 2 or 4, thus obtaining a 256×512 or 256×256 polar image. Since the number of available A-lines is usually 256, in order to reconstruct a full 360 degree tissue visualization, an interpolation task is needed. In order to complete the image reconstruction process, a simple linear interpolation and a Gaussian smoothing filter can be applied [12].

Material	Lung	Bone	Kidney	Liver	Brain	Fat	Blood	Water
$\alpha\ (dB/(MHz \cdot cm))$	41	20	1.0	0.94	0.85	0.63	0.18	0.0022

Table 1: Attenuation factors

4. Artifacts in IVUS

As commented before, the IVUS imaging technique is affected by some artifacts. We can split these artifacts in two classes: *static* and *dynamic*. The *static* artifacts are mainly two: the ring down effect and the guide wire shadowing. These two artifacts have been discussed in previous sections, and they actually depends only on the transducer manufactory process. The *dynamic* artifacts are caused by the heart beating. These artifacts severely affect the coronary inspection, thus they deserve to be discussed in details.

4.1. Dynamic properties of coronary IVUS pullbacks

To clarify how the *dynamic* artifacts affect the vascular inspection, it is worth to outline the standard procedure of data acquisition. Fig. **15** shows a schema of a classical IVUS acquisition setup. During the acquisition pro-

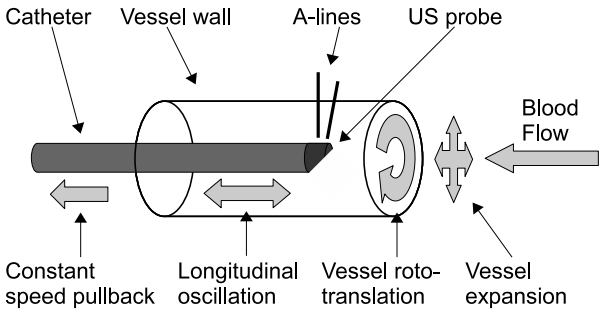

Figure 15: Schema of an IV US acquisition setup.

tocol, the catheter is pulled back (pullback) at a constant speed in order to acquire spatially subsequent images of the artery. In this way, theoretically, a trunk of the vessel can be sampled at regular spatial intervals. However, during this procedure, the heart beating produces artificial fluctuations of the probe position along the axis of the vessel. Moreover, due to the heart cyclic contraction/expansion, an apparent rotation with respect to the catheter axis and in-plane translation can be observed. Finally, due to the pressure changes, during the heart cycle, the vessel cyclically expands and contracts. Due to these motion phenomena, the appearance of the cross-sectional images can change significantly depending on the heart cycle phase.

Summarizing, IVUS pullbacks suffer from different *dynamic* artifacts: First of all, (1) the position of the transducer is not fixed with respect to the vessel morphology in the plane orthogonal to vessel extension, also called short-axis. This cause that subsequent frames in a motorized pullback can be misaligned. Moreover, (2) since the visual aspect of the vessel can change due to its elasticity and due to the heart motion, the IVUS sampling depends on the sampling instant with respect to the heart cycle. This causes that subsequent frames in the pullback can have different vessel size or relative position and/or rotation in the image plane. Finally, (3) the longitudinal movement of the transducer is affected by a continuous oscillatory movement due to the heart beats; this causes that some positions in the vessel are sampled multiple times, and the pullback presents an oscillation in the longitudinal direction that can be easily seen in the resulting pullback video.

4.2. Longitudinal swinging artifact

The longitudinal swinging effect can be mathematically modeled to better understand its behavior [13]. Let $V(l,x,y)$ be a virtual stack of all images that represents the vessel at each longitudinal position l. We can model the image formation during the pullback as:

$$I(t,x,y) = G(V(l_0 + s \cdot t + f(\phi(t)), x, y), \phi(t)) \quad (10)$$

where s represents the constant speed of the motorized pullback, $f(\phi(t))$ represents an unknown function that describes the longitudinal displacement as a function of the heart cycle phase (modeling in this way the artifact (3)). G represents an unknown 2D operator that describes the vessel image deformation due to the heart cycle, depending on the phase $\phi(t)$ (modeling artifacts (1) and (2)). The quantity $l_0 + s \cdot t + f(\phi(t))$ represents the position of the transducer in the vessel at time t. Equation (10) represents the catheter position as an initial value l_0 plus a constant speed s motion plus an unknown quantity f that depends on the phase $\phi(t)$. This formulation clarifies that the heart beating is the only cause of *dynamic* artifacts and that the key variable, that introduce periodicity in the artifacts magnitude, is the cardiac phase $\phi(t)$.

4.2.1. ECG based gating

The uneven sampling of the vessel structure (caused by (3)) can be reduced using a gating method. The gating is thought as a method to sample evenly spaced and stable frames. The stability refers to the fact that, after the gating, in subsequent frames the vessel should have a similar position and rotation. This theoretically permits to have a sampling that does not contain artifacts due to the heart cyclic movement. The gating can be performed *on-line*, but it requires a longer time of IVUS intervention for the physician and for the patient. Another possibility is to perform a motorized pullback

while capturing the ECG signal and then perform an *off-line* (also called *retrospective*) ECG gating. This technique heavily reduces the duration of the clinical exam while giving sub-optimal frames, since the frame rate is fixed, and we can sample only approximately at desired instants. Recently, other disadvantages of *off-line* ECG-gating have been highlighted: (1) the optimal sampling instant in the heart cycle is difficult to select (usually, the end-diastolic point) and it has high inter and intrapatient variability; (2) the ECG signal is a global measurement of the heart electrical activity while the artifacts due to the heart movement can change locally depending on the actual position of the catheter. These two points have been partially addressed in [14]. A new promising direction in IVUS *off-line* gating is to perform an image-based analysis of the pullback data and to infer optimal sampling points *without* considering the ECG signal.

4.2.2. *Computer assisted methods for longitudinal swinging artifact: Image-based gating*

As above mentioned, the image-based gating is a new promising direction to perform retrospective selection of stable frames. These methods make no use of the ECG signal and totally rely only on the information contained in the IVUS pullback. In [15] authors propose an algorithm that extracts the information on cardiac cycle by analyzing image sequence variation of two properties computed on a region of interest (ROI). The properties are the *Average Intensity* of the ROI and the *Absolute Intensity Difference* between ROIs of subsequent frames. In [16] authors discuss results of their Intelligate method showing that the method performs actually as good as an ECG gating technique. In [17] and [14] authors propose an image-based gating algorithm. The basic idea is to introduce the use of a dissimilarity matrix $\Phi(F_i, F_j)$ that measures the dissimilarity between the frames F_i and F_j of the same IVUS pullback, where i and j represent temporal variables. Once defined a proper measure such that $\Phi(F_i, F_j) \geq 0$, they obtain a matrix that exhibits a repetitive pattern of local minima and ridges of local maxima. The pattern is repeated so that some diagonals represent the loci of local minima, thus representing a specific interval between any two frames that present minimal dissimilarity; the principal diagonal is obviously not considered since $\Phi(F_i, F_i) = 0$. The first diagonal of local minima is displaced a number of columns; this displacement is a clue for detecting the average heart beat along the sequence. To enhance the sharpness of maximal ridges, they convolutes the matrix Φ with an X-shaped inverted Gaussian kernel obtaining a matrix $\hat{D}$. Now, local maxima on the above defined diagonal identifies couple of frames that have a high similarity and minimal inter-frame motion. Then, authors use two algorithms to select the best frames in the path on the diagonal that have the highest local maxima in $\hat{D}$. In [18] authors propose a method to extract the cardiac phase from IVUS sequences based on the hypothesis that the oscillation of the vessel wall is visible in longitudinal cuts. In [13], the authors modifies the method in [14] to make it more robust and computationally efficient.

4.3. *Short-axis oscillation*

The other main *dynamic* artifact is the short-axis oscillation and deformation. Fig. **16** shows two examples of longitudinal cut. The oscillation in the short axis can be noticed easily in the longitudinal cut as a saw-shaped oscillation of the vessel wall. This artifact negatively

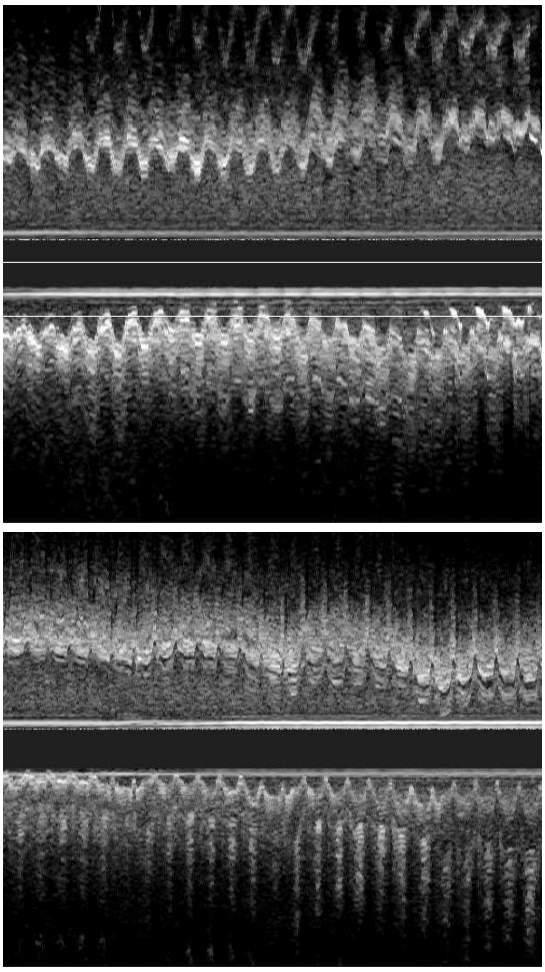

Figure 16: Two examples of longitudinal cut view.

impacts on the visual quality of the longitudinal cut; a visualization that is often used by clinician to quickly estimate the length of plaques and the degree of stenosis. In particular, the periodical rotation in the short-axis can cause that important structures, as e.g. a plaque, to appear and disappear periodically in the longitudinal cut (see Fig **16**, right). With the aim of alleviating the effect of this artifact on the longitudinal cut appearance, various computer assisted methods have been proposed so far.

4.3.1. Computer assisted methods for Short-axis oscillation reduction

The registration of IVUS images is a challenging topic mainly for two reasons: (1) IVUS images suffer from speckle noise and have poor definition of edges; (2) the vessel shape changes in a non-rigid way due to heart movement. The result is that the same part of the vessel can appear quite different if sampled at two different phases of the heart cycle. Different rigid and non-rigid registration algorithms have been proposed to tackle these two issues. In [19] the authors present a method for non-rigid alignment of IVUS image based on Generalized Correlograms (GC) [20]. The method applies anisotropic diffusion to the IVUS images and detects the vessel boundary using a snake. Then, the algorithm samples the boundary at different location to extract a set of local features. The non-rigid transformation is estimated by finding the optimal set of correspondence between landmarks (GC) of two IVUS images. The method is highly computational demanding and has been conceived to perform non-rigid registration aimed at retrieval. An alternative method to suppress IVUS image rotation based on a kinematic model is presented in [21]. The model is used to estimate the center of rotation in the short-axis by computing the rotation of two ellipses that fit the vessel border in the two compared images. The method requires detection of the vessel border with sufficient precision using a trained neural network. In [22], a rigid registration algorithm composed of two steps is presented. Firstly, the method fixes the center of rotation as the center of mass of image gray scale values. Secondly, it estimates the rotation between the two images by spectral correlation analysis [23]. The most important limitation of this method is that the estimation of rigid rotation heavily depends on correct estimation of the center of rotation. In our opinion, the center of mass, while robust with respect to noise and changes in image texture, is not a good estimate of the center of rotation. In [24], the authors present a method based on the scale-space optical flow algorithm with a feature-based weighting scheme. The algorithm has been tested on a tissue-mimicking phantom, subjected to controlled amounts of angular deviation. While interesting, the approach estimates only the catheter rotation, which point of rotation is fixed in the image center. Recently, in [25], the authors proposed a method that aims at registering subsequent IVUS images by aligning the center of the vessels first, based on a modified version of the Fast Radial Symmetry transform [26]; and then estimate the relative rotation by spectral correlation analysis [23]. The algorithm is also sufficiently efficient and highly robust to intra-patient variations. The method has shown to outperform the one in [22], having similar computational cost. Fig. **17** shows an example of longitudinal cut before and after the registration using the method in [27]. It can be noticed that the sequence has been registered such that the lumen appears as an horizontal tube; moreover, the registration allows to clearly see the length and thickness of the plaque and the adventitia border.

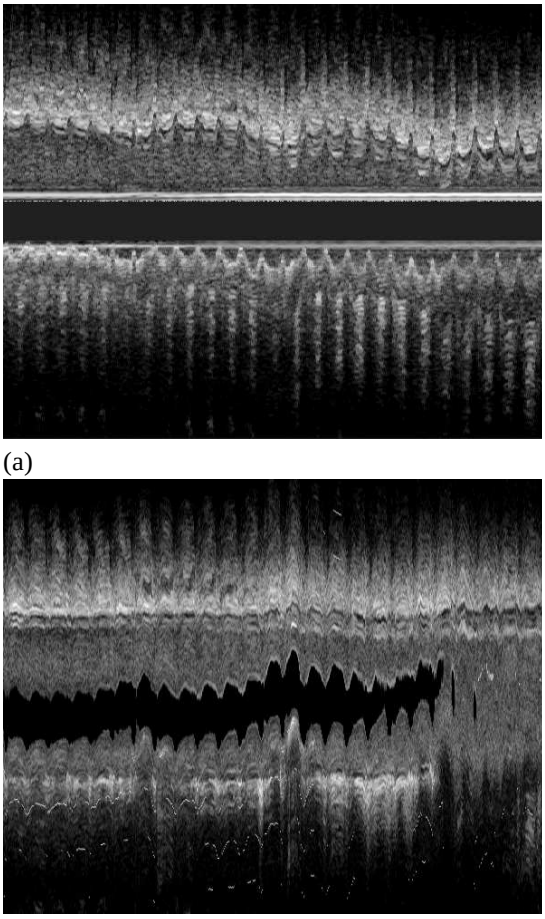

(a)

(b)

Figure 17: An example of a longitudinal cut before (a) and after (b) applying the registration method described in [25]

5. IVUS-BASED PLAQUE CHARACTERIZATION

One of the most important property of IVUS modality consists in its ability of describing the inner morphology of the vessel and, moreover, its tissue composition. As depicted in section (2), different tissue types show different acoustic properties (see Eq. 2) and, consequently, different intensity and shape of the reflected ultrasonic wave; furthermore, the contribution of the scattered component is also different for each tissue. As results, in the IVUS image, areas corresponding to different tissues exhibit different grey-level intensity and textures. Plaque characterization problem actually consists in a *pattern recognition* problem. For this reason, in each one of the method proposed in the last 10 years, the main steps of a pattern recognition problem can be distinguished: (1) ground truth collection, (2) feature extraction and (3) training of a classifier.

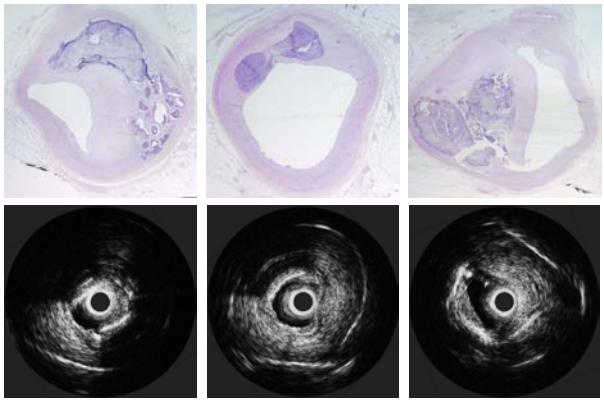

Figure 18: Pairs of images obtained by histological analysis (above) and corresponding (below) IVUS image

5.1. GROUND-TRUTH COLLECTION

The main goal of each automatic plaque characterization technique consists in training a mathematical model called *classifier* with a set of examples. In the tissue characterization problem, the classifier is fed with examples of different plaque types, like the *calcified*, *lipidic*, *fibrotic* and *necrotic* one. Basing on the features of the training examples, the classifier should be able to correctly recognize new unknown examples by comparing their feature with the features of the learned cases. It is clear that the set of examples used to train the classifier must be extremely reliable, since an error in this database causes a systematic misclassification.

In pattern recognition problems, the training set is called *ground truth*, consisting in a reliable data-base of labeled examples of the objects we want to recognize. The ground truth is typically used during the training task but also during the validation task, when the quality of the trained classifier must be assessed.

In the atherosclerotic plaque characterization problem, the gold standard procedure for producing a reliable ground truth is the histological analysis of post-mortem cases. Given an ex-vivo coronary artery is in fact possible to acquire IVUS data and then, by an histological analysis, to correctly determine the nature of each atherosclerotic plaque found into the artery (Fig. **18**). In this way, a team of experts together with pathologists can establish the correspondence between the plaque area encountered in the histology and its corresponding representation on the IVUS image. The *labeling* process is then performed, consisting in assigning a different label to data corresponding to different tissue types, and the ground-truth is created. During this process, the use of a software that deforms the histological image in order to match the IVUS image can be also used [28].

In almost all the methods proposed in recent years, the histological analysis is used to create the ground-truth and the discriminative power of the characterization methods is assessed with ex-vivo cases, under the assumption that differences in data from ex-vivo cases and in-vivo cases are negligible.

Alternatively, a ground truth can also be created by using data from in-vivo examples. In this case, the labeling process is performed by experts without the information provided by histology. No assumptions on the differences between data used as ground truth and data from clinical cases are needed in this case, but the reliability of the obtained ground truth is relied only on the experience of physicians.

5.2. FEATURES EXTRACTION

Once the ground truth has been created, the data features extraction is performed. Basing on the idea that different tissues produce different echoes, several approach for extracting features from IVUS signals have been proposed. Early approaches were based on the analysis of texture and patterns on the IVUS image produced by the IVUS equipment, while more recent approaches are focused on the analysis of raw radio frequency signals extracted from the catheter. The main approaches, based both in texture and RF signal analysis, are now presented.

5.2.1. TEXTURAL FEATURES

In textural features approaches, the input data consists in the IVUS image, expressed as a two variables discrete function $I(x,y)$, thus treated as a matrix. The first plaque characterization method based on the analysis of the texture of the image is presented in [29]. Starting from a large set of textural features (histogram contrast, skewness, kurtosis, dispersion, variance, radial profile, energy, entropy, maximum probability, contrast, inverse difference moment, short primitives emphasis, long primitives emphasis and brownian fractal dimension), the features with the highest discriminative power are identified using the inter-class distance search criterion and the Euclidean metric, thus using:

- **Radial profile** It is a gray-level-based texture descriptor, oriented to reflect the different gray level profile characteristics of the hard and soft plaque. For an elementary region with a point of interest at (x_1, y_1) the radial profile is determined as

$$\rho_{profile} = \frac{I(x_1, y_1)}{max_{\Delta y} I(x_1, y_1 + \Delta y)} \tag{11}$$

  where $\Delta y = 10, 20, \ldots, \Delta y_{max}$, and Δy_{max} is given by the image size.

- **Long-Run emphasis** It is a measure describing the maximum contiguous set of constant gray level pixels located at a specified direction: a large number of neighboring pixels of the same gray level represents a coarse texture, a small number of these pixels represents a fine texture and the lengths of

texture primitives at different directions can serve as texture descriptor.

- **Fractal Dimension** This measure is calculated through the transformation of image space to fractal dimension.

Despite of the high accuracy achieved, the main problem of using the IVUS images obtained with the IVUS equipment is the lack of normalization in data they provide. In order to improve the tissue visualization, in fact, usually physicians need to change the imaging parameters of the IVUS equipment, like contrast, depth, gain etc. In this way, the same tissue observed into two IVUS images acquired with different imaging parameters set presents different features.

In order to extract coherent and comparable features belonging to different tissue, a set of normalized IVUS images should be used. For this purpose, the raw radio frequency signals captured by the IVUS equipment can be exploited to reproduce the image formation process, with a unique and well controlled set of imaging parameters [30]. Furthermore, using the Raw RF signals as basis for the reconstruction, guarantees a lack of different gains applied to the signal itself. In [30] the reconstruction process is used to create a set of IVUS images of in-vivo cases in which experts segment atherosclerotic plaques. Textural features are then extracted by using:

- **Co-occurrence matrix** It can be defined as an estimation of the joint probability density function of gray level pairs in an image. The element values in the matrix are bounded from 0 to 1 and their sum is:

$$\begin{aligned} &P(i, j, D, \theta) = P(I(l, m) \\ &= i \otimes I(l + D\cos(\theta), m + Dsin(\theta)) = j), \end{aligned} \tag{12}$$

  where $I(l, m)$ is the gray value at the pixel (l, m), D is the distance among pixels and θ is the angle of each its neighbor. Given the co-occurrence matrix it is possible to compute a set of second-order statistic measures of texture, like the *energy*, *kurtosis*, *entropy* etc.

- **Local Binary Patterns** LBSs are used to detect uniform texture patterns in circular neighbourhoods with any quantization of angular space and spatial resolution. They are based on a circular symmetric neighborhood of P members with radius R. To achieve gray level invariance, the central pixel g_c is subtracted to each neighbor g_p, assigning the value 1 to the result if the difference is positive and 0 otherwise:

$$LBP_{R,P} = \sum_{p=1}^{P} a(g_p - g_c) \cdot 2^p, \tag{13}$$

  where the operator $a(x) = 1$ if $x > 0$ and 0 otherwise.

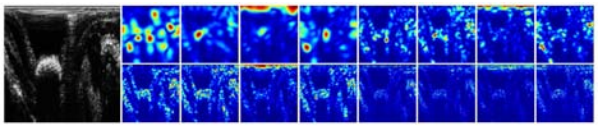

Figure 19: Bank of 16 Gabor filters, obtained by varying the angle and the frequency, applied to the IVUS image in polar coordinate. Note that the tissue vary their response when different filters are applied

- **Gabor Filters** It is a special case of wavelets and can be defined as a Gaussian g modulated by a complex sinusoid s. In 2D, a Gabor filter has the following form in the spatial domain:

$$\begin{aligned} &h(x, y) = \tfrac{1}{2\pi\sigma_{x'}\sigma_{y'}} \\ &\cdot \exp\left\{-\tfrac{1}{2}\left[\left(\tfrac{x'}{\sigma_{x'}}\right)^2 + \left(\tfrac{y'}{\sigma_{y'}}\right)^2\right]\right\} s(x, y), \end{aligned} \tag{14}$$

  where $s(x, y)$ and the gaussian rotation are defined as: $s(x, y) = \exp[-i2\pi(U_x + V_y)]$, $x' = x\cos\theta + y\sin\theta$, $y' = -x\sin\theta + y\cos\theta$. x' and y' represent the spatial coordinates rotated by an angle θ. $\sigma_{x'}$ and $\sigma_{y'}$ are standard deviations for the Gaussian envelope. The aspect ration λ and its orientation are defined as: $\lambda = \frac{\sigma_{x'}}{\sigma_{y'}}$, $\phi = \arctan V/U$ where U and V represent the 2D frequencies of the complex sinusoid. Fig. **19** depicts an example of a bank of 16 filters applied to an IVUS image.

5.3. RF-BASED FEATURES

In greyscale IVUS, the backscattered signal is processed in real-time into a two-dimensional video image. This processing task introduces a certain set of approximations and also reduces the resolution in visualizing tissues. The approximate envelope of the RF signal is in fact computed first, followed by a subsampling process (usually by a factor 4) that reduces the number of sample in order to create an IVUS image of reasonable dimensions. The signal intensity is then discretized among 0 and 255 to be converted into greyscale image. Finally, the cross-sectional image creation requests an interpolation task that contributes in decreasing the quality of tissue representation. Therefore, even though reconstructed according to a standardized imaging parameter set, greyscale IVUS can be seen as a suboptimal tool to accurately and reproducibly identify plaque composition [31].

RF data from the unprocessed backscattered ultrasound signal provides an alternative to greyscale image analysis. Theoretically, analysis of the IVUS-RF data provides a more accurate and reproducible technique for measuring tissue properties because it is not subject to machine-dependent processing, subsampling, interpolation, quantization and even operator-dependent settings [31].

For this reason, post-processing of the backscattered (reflected) RF IVUS signal has been developed in order to better characterize plaque composition, since the ultrasound RF signals provide quantitative information on tissue microstructures [32]. Several approaches for features extraction from the Raw RF signals have been proposed.

ACOUSTIC IMPEDANCE (Z)

Given the relationship between the acoustic impedance ζ and the tissue density ρ (Eq. 2) and given that the US wave propagates with different velocity in different tissues, the relative acoustic impedance can be used as a parameter to classify plaque types [33]. This method assumes ultrasound pulse to be well approximated by using the Plane Wave Born Approximation (PWBA) deconvolved inverse scattering technique [34]. Given the matrix of US acquired A-lines, a Region of Interest can be selected and then windowed with a Hamming window of length equal to the length of ROIs. To each ROI a Fourier transform can be associated by averaging the spectra of all scanlines within the ROI. For each ROI, the value of the impedance relative to that of water can be computed following next steps:

- the ultrasound wave reflected from an ultrasound reflector (acrylic phantom) is acquired and reversed in the time domain: the incident pulse is then obtained;
- given the incident pulse, the reflection coefficient Γ (Eq. 6) is calculated as the ratio of the conjugate of the Fourier transform of the reflected pulse and the Fourier transform of the incident pulse itself;
- impulse response (IR) is obtained by calculating the inverse Fourier transform of the reflection coefficient. Relative impedance is then calculated using:

$$\zeta' = exp\Big(-\sqrt{2/\pi}\sum IR\Big) \tag{15}$$

POWER SPECTRUM

Based on the hypothesis that different tissues behave differently in the frequency domain, several approaches based on the analysis of power spectrum have been proposed. Mainly, for each ROI of N_r samples and M_r contiguous A-lines, a power spectrum can be associated to each point by averaging the power spectra computed in the lines belonging to the ROI. The power spectrum can be computed by means of the Fourier transform [35, 36, 37] or by using the AutoRegressive Model (ARM) [38, 39, 30, 40].

Basically, ARM are defined as a linear equation where the value of a stochastic process (A-line) x at a certain point t is equal to a linear combination of its p previous outputs weighted by a set of parameters:

$$x(t) = \sum_{k=1}^{p} a_k(k)x(t-k), \tag{16}$$

where p is the ARM degree and the coefficients a_k are calculated minimizing the error of the modeled process with respect to the original one using the Akaike's error prediction criterium. By means of the obtained values a_k it is possible to accurately estimate the power spectral density of the considered signal. The use of ARM is preferred in cases where the window size of the ROI is small, since in this case the technique provides a more accurate spectral approximation.

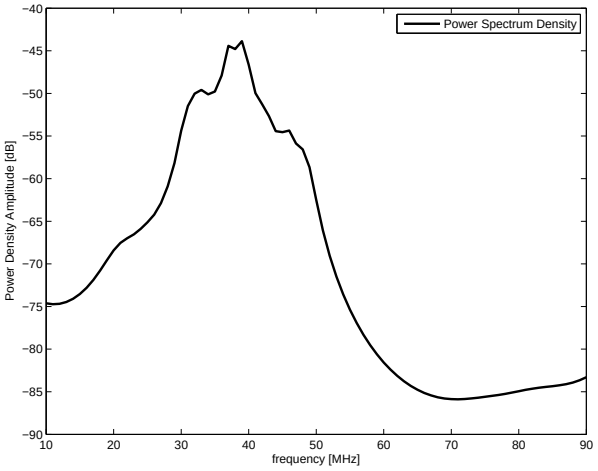

(a)

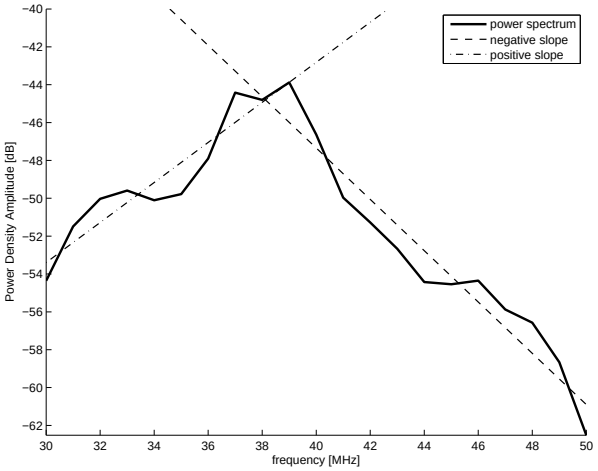

(b)

Figure 20: (a) Power spectrum of a ROI computed by ARM; the frequency range is 0-100MHz and the central frequency is 40MHz. In (b) the straight lines used to compute the spectral features are shown; in this case the frequency range is 30-50 MHz

Given the power spectrum, a set of spectral features can be extracted. Some features have been successfully used in plaque characterization techniques, as the mean power (dB), maximum power (dB), spectral slope (dB/MHz) (a least -squares linear regression over the given bandwidth), y-axis intercept of spectral slope (dB) (intercept of the straight line with the y-axis at 0 Hz) [35]. In addition, the value of the frequencies corresponding to maximum and minimum power can be used

[38, 39]. These features are extracted in a frequency range of 17-42 MHz, corresponding to the -20 dB bandwidth of the system. This set of features, commonly known in literature as the *seven-features* approach, together with the Integrated Backscatter (IB) represent the basis of a commercial product called *Virtual Histology* (VH), implemented in the Volcano (Rancho Cordova, CA) IVUS clinical scanners that offer near-realtime tissue characterization in vivo [32].

Alternatively to the presented spectral features, a *full-spectrum* approach can be considered [37, 36]. The use of a full-spectrum analysis demonstrated to produce more accurate results, when compared with the seven-features approach, when classifying fibrolipidic, lipidic, fibrotic and calcified tissue: when using a 40MHz catheter in fact, a lot of variations can be found in the main bandwidth of the signal (20-60MHz), thus justifying a full-spectrum analysis [37]. In the full-spectrum approach the power spectrum, with frequency range from 0 to 100 MHz, is discretized by using a certain number of bins and then used as feature vector for each point (the center of a ROI).

INTEGRATED BACKSCATTER (IB)

Integrated Backscatter (IB) is another feature, derived from the RF signals, that has been used in plaque characterization approaches [41, 42, 43]. The first method based on IB was proposed in 1989 and was oriented to the detection of acute myocardial infarction and reperfusion via M-mode echocardiography [44]. The IB is an intrinsic parameter of the electrical US signal and can be computed as [41]:

$$IB = 20 \log \left(\frac{\frac{1}{T} \sum_0^T V^2}{\frac{1}{T} \sum_0^T V_0^2} \right) \tag{17}$$

where V is the signal voltage from ROI, V_0 is the smallest signal voltage that the system can detect, and T is the integration interval.

It has been shown that the IB parameter combined with two-dimensional echo can differentiate the tissue characteristics in both in vivo and ex vivo studies [41, 42]. In Table 2 the computed value of the IB parameter when characterizing tissues in *in-vitro* cases are presented when discriminating calcifications, mixed lesions, fibrous tissue, lipidic core and thrombus. Since no overlaps in the obtained values are encountered, the discriminative power of this parameter is confirmed.

Histology	IB [dB]
Calcified tissue	$-30 < IB \leq -23$
Mixed lesion	$-55 < IB \leq -30$
Fibrotic tissue	$-63 < IB \leq -55$
Lipidic core	$-73 < IB \leq -63$
Thrombus	$-88 < IB \leq -80$

Table 2: Integrated Backscatter values obtained by histological analysis of post-mortem tissues. The values are provided as mean value ± 1 dB. Data extracted from [42]

A plaque characterization system based only on IB parameter is presently distributed only in Japan and uses the IVUS catheter from Boston Scientific based on a 40MHz single rotating crystal. Comparisons of IVUS-IB with histopathology demonstrated a high sensitivity for characterizing calcification, fibrosis, and lipid pool [32]. Finally, the IB parameter also represents the 8th feature of the Virtual Histology system [39].

WAVELET-BASED APPROACH

The wavelet analysis of RF signals has been also studied in recent years [45, 46]. A wavelet is mainly a waveform of limited duration and zero average amplitude [47] while the *wavelet analysis* is one of the time-frequency domain analyses of signals, extracting a unique local wave pattern within a complex original IVUS-RF signal by iteratively computing wavelet coefficients that are localized by the amplitude and the position of wavelets.

The hypothesis in this kind of approach is that the IVUS-RF signal belonging to different tissues exhibits different behavior when analyzed by wavelet, and that the wavelet coefficients, computed at different scales, could be the discriminative measures to be used in the tissue characterization [31].

This approach has been proved to be appropriate in discriminating the fibrous from the fatty areas within atherosclerotic plaques [45], thus demonstrating the useful use of wavelet coefficients.

ELASTOGRAPHY-BASED APPROACH

The last interesting approach that we consider is based on elastography, i.e. the measure of the stiffness of a tissue. From equation 2 we see that the stiffness value of a tissue is indicative of its histological composition. Hence, the hypothesis at the basis of this approach is that the measure of the tissue stiffness, actually consisting in its strain map, can be used as a discriminative parameter to discriminate tissues [48, 49, 50, 51, 52, 53].

In order to obtain the strain map of a tissue by ultrasound, the area containing the tissue must be first imaged at two different pressure conditions. After that, the so called pre-compression and post-compression images are correlated and regions with large and small change in positions are then detected: this is called the shift-diagram. Finally, the strain diagram can be obtained by deriving the obtained shift-diagram.

This approach has been successfully applied to detecting fatty plaques in *ex-vivo* [49, 48] and *in-vivo* [50] cases. Usefulness of elastography has been also demonstrated in plaque modeling of aortic artery in rabbits [53] and potentially useful for 3D field extensions [52].

6. CLASSIFICATION/CHARACTERIZATION

Once the features are extracted, a certain description of the tissue is defined. Given the collected ground truth

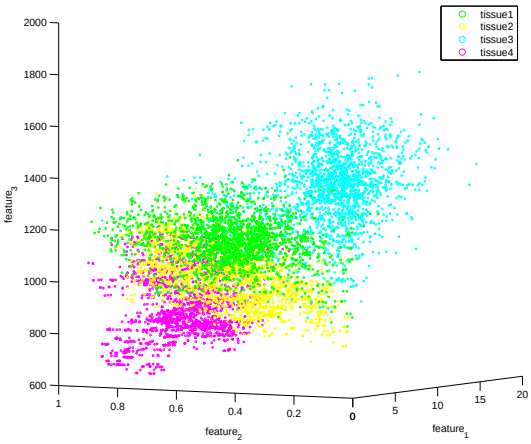

Figure 21: Feature space. A set of point acquired from 4 different tissue types are represented in the space of 3 discriminative features.

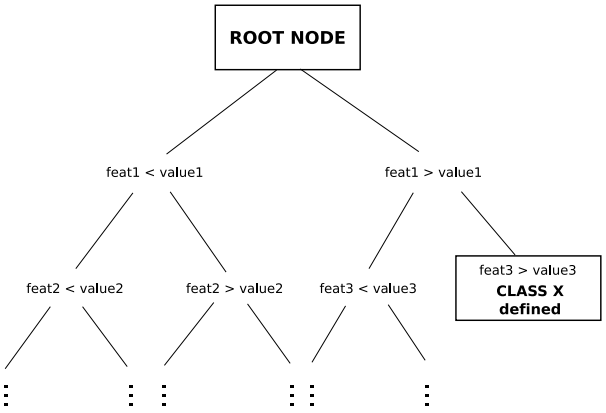

Figure 22: Decision tree. Starting from the ROOT NODE, at each node the most discriminant feature is computed, thus defining the "path" to the recognition of each class

it is also possible to assign a reliable label to each one of the set of data relative to atherosclerotic plaques. The set of labeled data is then passed as input to a mathematical model called *classifier* for the training process.

A classifier actually is a probabilistic model (discriminative or generative) with a set of parameters determined (learned) during the training process. The model is in fact able to learn the characteristics of the input data, from their features, and to set its parameters according to data. When the training process is over, the set of learned parameter is finally saved and the classifier is ready to be used to characterize unknown examples.

The atherosclerotic plaque characterization problem implies the definition of a multi-class classifier. Except for some approaches that aim to discriminate for example fibrotic from fatty (lipidic) plaques, the main scenario implies the discrimination among fibrotic, lipidic and calcified plaques. Furthermore, the necrotic core, fibrolipidic and lipidic with calcifications tissues are also considered in some approaches. The characterization problem actually consists in separating, in the feature space, clouds of points belonging to multiple classes (Fig. **21**).

Several approaches have been presented to solve the multi-class tissue characterization problem: we will refer to them with the word "architecture", since actually they often consist in combining a set of simple classifiers into a more complex framework.

6.1. DECISION TREE

One simple architecture for the discrimination of different tissues is the *decision tree* [38, 39]. Starting from a main node (root), during the training process, at each node the input data are split into sub-groups according to the most discriminative feature in that node. For example, starting from the root node, during the training process we can find that a certain $feat_i > value_i$ is mainly a property of some tissues, while a $feat_i < value_i$ for the same feature is related to other tissues. By proceeding in this way, the discriminant features and their value are defined at each node (Fig. **22**). When a new unknown example must be classified, its features are then simply compared, at each node, with the threshold set during the training process, thus assigning it a label. Several techniques can be used to assign the most discriminant feature to a node and to define its value. The most important are based on the *Entropy*, the *Information Gain*, the *Gini Index* and the *Partition Distance*.

6.2. ERROR-CORRECTING OUTPUT CODE

Another effective approach for the solution of multi-class plaque characterization problem is the use of Error-Correcting Output Code (ECOC) technique [30, 54, 12, 40].

ECOC [55] is a technique that combines N binary classifiers to solve a K-classes classification problem. A binary classifier is a model trained to discriminate among two set of data. Given an unknown example as input, the binary classifier is able to label it as belonging to the class 1 or to the class 2, thus producing a +1 or -1 output value, respectively. For each class a particular *codeword* $c_k = \{1, -1\}^{1\times N}$ is obtained ($k = 1, ..., K$). Based on a chosen coding strategy, a matrix $\mathbf{M} = \{1, 0, -1\}^{K\times N}$ is designed (Fig. **23**), in which each column represents a binary classifier H_j (*dichotomy*) and each row represents a class. A value 1 in position $\mathbf{M}(k, j)$ means that the j^{th} dichotomy classifies an unknown example as belonging to the class k, a value -1 means that it belongs to the class $q \neq k$ and a 0 value means that we do not care about classification result, regarding class k. Therefore, to classify an unknown example, the distance between the obtained codeword and each row m_k of the matrix $\mathbf{M}$ is computed: the inferred class is the value k reporting the minimum distance. Different *coding* tech-

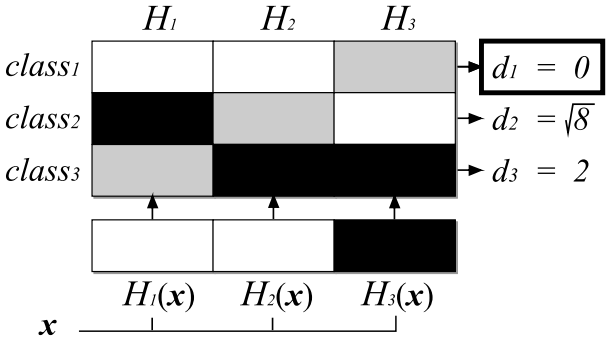

Figure 23: ECOC matrix for a 3-class problem, One-vs-One coding technique and Attenuated Euclidean Decoding (AED) technique; the distances value are showed for each row of the matrix

nique can be used. The most popular is the *one-vs-one*, in which each pair of classes is considered an the respective classifier trained. Alternatively, a *one-vs-all coding* can be used, where each class is discriminated towards the other classes. For the *decoding* technique, different distance measures can be used. The most common are the Euclidean and the Hamming distance.

The benefits in using an ECOC framework are mainly (*i*) the possibility of combining several binary classifiers into a multiclass framework, (*ii*) the automatic error-correction property of ECOC of correcting some errors in the prediction and finally (*iii*) the flexibility of a multi-class architecture in which several variations, like the sub-class classification [54] can be easily adopted.

6.3. ENSEMBLE ARCHITECTURE

The last multi-class architecture we are going to present is the Ensemble framework [36]. Usually, during a standard training process, a classifier is trained, in order to learn parameters according to input data. We can call it an “expert” for that particular data characterization problem. The main idea of an ensemble architecture consists in using several experts, instead of one, i.e. several classifier, trained to solve the same problem.

According to the combination policy of these experts different ensemble architectures can be built. Two of the most popular ones are *boosting* and *bagging*. The *boosting* procedure combines experts in an incremental way. Given a set of experts, at each step of the boosting process a new expert is added to the ensemble so that it focusses on data that was previously misclassified. This selected set is usually combined by means of a weighted additive model.

Another important family of ensembles comes from the *bagging* process. This process specializes each expert on a different sampling of the data set. Then, by means of voting procedure these experts are combined. This process results in very robust classifiers. For example, in the problem of discriminating the fibrotic from the rest of tissues, N binary classifiers are trained: each classifier is trained with a set of data randomly selected, with reinsertion, from the original training dataset. Hence, M classifiers are obtained for each binary problem, and each one of them shows a certain classification accuracy, depending on how the randomly selected dataset is representative of the global training dataset: this accuracy is somehow taken into account by weighting the result of each single prediction with the weight s_i. Then, in order to discriminate a tissue, a combination of the predictions of the M classifiers is considered; this combination can be seen as a monolithic macro-block (array) for the detection of this particular tissue (Fig. **24**). In the multi-class classification problem, following the bagging architecture, this blocks are repeated N times for each considered tissue, thus generating the final predicition on an unknown example by further combining the predictions of each macro-block.

Similarly to that exhibited by the ECOC framework, this approach embeds a kind of error correction capability, given by the contribution of several ”experts” and by the combination of their ”opinions”. Furthermore, the architecture foresees the use of a large number of macro-blocks ($M \times N \times K$) and though this fact decreases the probability of error, it increases the computational time.

7. RESULTS

The last step in the design of a plaque characterization model consists in its *validation*. This task is common to each medical data processing methodology and, more in general, to each pattern recognition model, requiring (1) the creation of a highly reliable data set to be used to test the discriminative power of the designed method and (2) a mathematical testing procedure to follow in order to obtain reliable results. This last procedure is commonly known as *cross-validation*.

7.1. In-vitro data validation procedure

As mentioned in section 5.1, the gold standard procedure for obtaining a validated ground truth in the tissue characterization problem consists in the histological analysis of post-mortem arteries. In order to extract IVUS data, the artery (separated from the heart) is first fixed on a mid-soft plane and filled (using a catheter) with physiological saline solution at constant pressure (around 100 *mmHg*), simulating blood pressure. In the panel the distal and proximal position, together with left and right hand are marked to be used as a reference for the marker position. The probe is then introduced and RF data are acquired in correspondence of plaques. These positions can be clearly marked on the external part of the artery. The artery is then cut in correspondence of previously marked positions and plaque composition is determined by histological analysis.

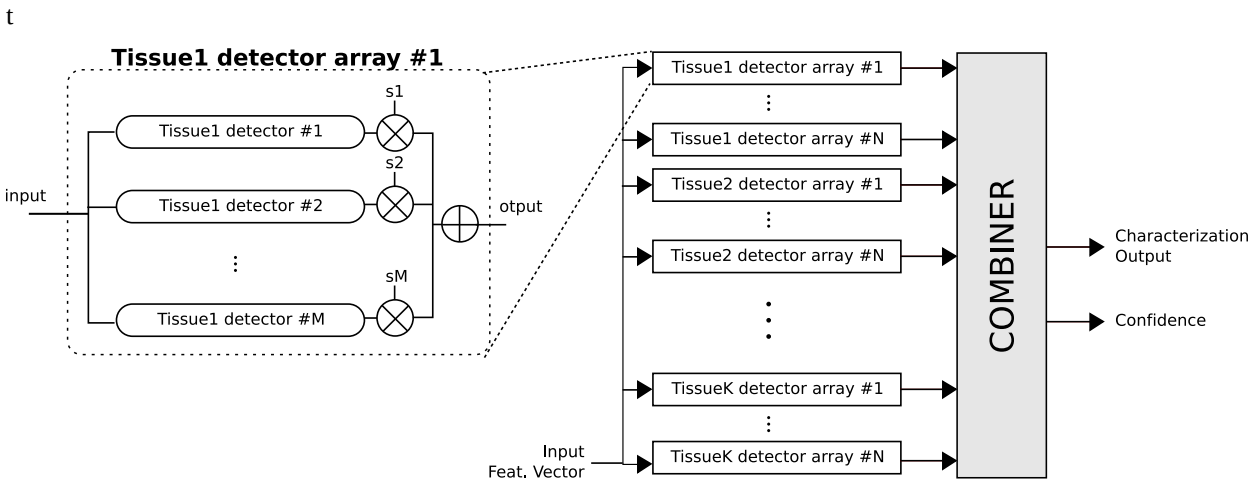

Figure 24: Bagging/Ensemble architecture. Given the number of K classes, an array of M binary classifiers is constructed. Their prediction is combined taking into account the classification reliability s_i of each one. The output is then repeated N times for each one of the K classes and then combined to produce the output. Optionally, a classification confidence measure can be obtained

As alternative, a specially designed box containing the artery can be used, allowing to automatically cut the vessel at a fixed number of positions by superimposing a dedicated set of knives [37]. With this procedure, a set of equally-spaced artery cuts are obtained.

For each cut, an image of the tissue obtained by using a microscope is obtained. Given the reference points in the panel and in the IVUS image orientation it is possible to put in correspondence the plaques detected by histology with their respective areas in the IVUS image. This task is achieved by the joint cooperation of expert physicians together with pathologists. The different conditions and modalities in which the two images are acquired are profoundly different. The mechanical consistence given to the artery while acquiring IVUS data is lost in the moment of cutting the vessel. Phenomena of tissue spoiling and a certain error in finding the exact correspondence between the IVUS and histological image make hard to get a good registration and, consequently, a reliable automatic labeling. Hence, the labeling process can be performed manually by joint cooperation of experts and pathologist or by using a dedicated software able to register the two images obtained by different modalities and different approaches [38, 39], and the ground truth is thus obtained.

7.2. Cross-validation

Validated IVUS data are obtained from a set of ex-vivo cases. Even though they actually consists in post-mortem cases, the intra-patients variability in data properties is still applicable. For this reason, the procedure of validating the discriminative power of the proposed method must be carefully assign data of different patients to the training and the validation data set. The training data set represent in fact the set of data used to train the

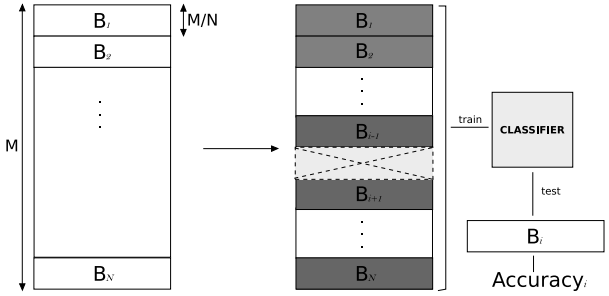

Figure 25: Data division while performing N-fold cross validation. M is the number of data examples, N is folds number

classifier, while the validation data set is used to assess the discriminative power of the trained classifier. It is clear that when the classifier is used to characterize examples of the training set, the classification error tends to zero, since the discriminative bounds in the feature space have been actually modeled on that data. For this reason, it is extremely important that no examples of the validation data set is included in to the training data set.

Furthermore, in order to obtain completely reliable numerical values, the testing phase must be repeated a certain set of times (rounds) and then statistical results must be extracted.

N-fold cross-validation The most common cross validation technique is called *N-fold cross-validation*. It consists in considering the whole available data set (actually the available ground truth) and dividing it into N parts (blocks) containing the same number of data examples. A classifier is then trained by using $N-1$ blocks and its discriminative power is assessed by testing in the remaining block. This process is repeated

N times and, after repeating several rounds, the final classification performance are given as mean value and standard deviation of the obtained results.

The performance parameters typically considered in a plaque characterization problem are:

- Accuracy (A) = $\frac{TP+TN}{TP+TN+FP+FN}$
- Sensitivity (S) = $\frac{TP}{TP+FN}$
- Specificity (K) = $\frac{TN}{TN+FP}$
- Precision (P) = $\frac{TP}{TP+FP}$

where TP = true positive, TN = true negative, FP = false positive and FN = false negative.

Among the N-fold cross-validation techniques, the 10-fold and the 5-fold [56] are largely used. Even though this technique can be successfully used to assess reliable results, one of the common error consists in the creation of the *N* blocks. It is common in fact to create the sub-data sets by randomly sampling the whole data set, without re-insertion, or even by simply dividing by a factor N the sequential set of all the available examples. In this way, the complete separation between the training and the validation data set is not assured, since it is impossible to control the random selection process; furthermore, since the number of examples contained in each patient may not be constant, the sequential division of the whole data set could mix part of a validation case with the other ones.

For this reason, a technique that has been recently considered is the so called *Leave-One-Patient-Out* (LOPO). It can be considered as a special case of the N-fold cross-validation, where *N* now consists in the number of necro cases and each block actually consists in the set of all examples of each individual case. In this way, the complete separation between the training and the validation set is assured, and the intra-patients variability is taken into account. For these reasons, the results provided by the LOPO technique can be considered as indicative of the behavior of the designed model in presence of a new unknown clinical case. During the cross-validation method in fact, the validation case is, respect to the classifier, a completely unknown case.

7.3. Classification results

In almost all the proposed plaque characterization techniques, an overall accuracy between 80% and 92% is achieved. The main discriminated tissues are the fibrotic, lipidic and calcified tissue. Furthermore, mixed tissue like fibro-lipidic, lipidic with calcification and fibro-calcified tissue have been also considered in some approaches, together with the necrotic core and the thrombosis. In Fig. **26** an example of fibrotic, lipidic and calcified tissue characterization is presented, computed by using the database in [12]. The sensitivity parameter is depicted, after 5 rounds of LOPO cross-validation technique, and 10 test cases have been randomly selected from the validation data set.

One of the main problem in the tissue characterization, highlighted in Fig. **26** as well, is commonly admitted as the misclassification between lipidic and fibrotic plaque. Furthermore, phenomena of misclassification are also experimented between calcified and necrotic tissue. These phenomena can be observed when computing the confusion matrix of the classified examples. In some cases, this problem is solved by considering the pairs of misleading (different) tissues as a unique tissue type, thus reducing the classes number in the multi-class problem definition [39]. In order to solve this problem, recently an approach based on sub-class tissue definition has been presented for a three tissue plaque characterization approach [57].

Another commonly assumed problem consists in the difficulties of classifying tissue beyond the calcified plaque. Since the calcified tissue presents a high echo-reflectivity property, the US wave does not go through the tissue itself, thus generating a *shading* effect resulting in very low signal intensity area, corresponding to a black area in the IVUS image, beyond the plaque. The difficult in observing a signal beyond the plaque does not imply that no plaque can be actually encountered beyond the tissue. For this reason, the problem of "classifying beyond the calcium" is still an open problem [58].

References

[1] G. K. Hansson, Inflammation, atherosclerosis, and coronary artery disease, N Engl J Med 353 (2005) 429–430.
[2] M.Madjid, A.Zarrabi, S.Litovsky, J.T.Willerson, W.Casscells, Finding vulnerable atherosclerotic plaques. is it worth the effort?, Arterioscler Thromb Vasc Biol. 24 (2004) 1775–1782.
[3] G. Gorge, J. Ge, D. Baumgart, C. von Birgelen, R. Erbel, In vivo tomographic assessment of the heart and blood vessels with intravascular ultrasound, Basic Res Cardiol. 93(4) (1998) 219–40.
[4] S. E. Nissen, P. Yock, Intravascular ultrasound: Novel pathophysiological insights and current clinical applications, Circulation 103 (2001) 604–616.
[5] W. Schaberle, Ultrasonography in Vascular Diagnosis, Springer, 2004.
[6] S. G. Ellis, D. R. H. jr. (Eds.), Strategic approaches in coronary intervention (3rd Edition), Lippincott Williams & Wilkins, 2006.
[7] R. J. Siegel (Ed.), Intravascular Ultrasound Imaging in Coronary Artery Disease, 1998.
[8] S.Sethuramana, S.R.Aglyamova, J.H.Amirianb, R.W.Smallingb, S.Y.Emelianova, Development of a combined intravascular ultrasound and photoacustic imaging system, Proceeding of SPIE 6086.
[9] E. Ascher (Ed.), Vascular Surgery (5th Edition), Blackwell, 2003.
[10] G.Bianchi, R.Sorrentino, Electronic filter simulation & design, 2007, p.17-20.
[11] R.C.Gonzalez, R.E.Woods, Digital Image Processing (Second Edition), Addison-Wesley, 2001.
[12] F. Ciompi, Ecoc-based plaque classification using in-vivo and ex-vivo intravascular ultrasound data, Master thesis (2008) (in printing).

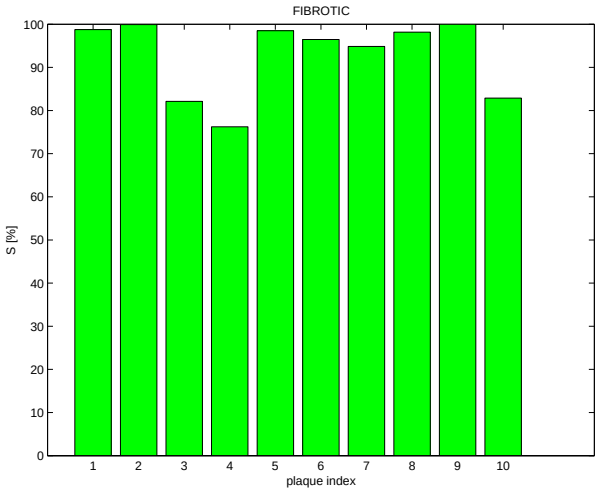

(*a*)

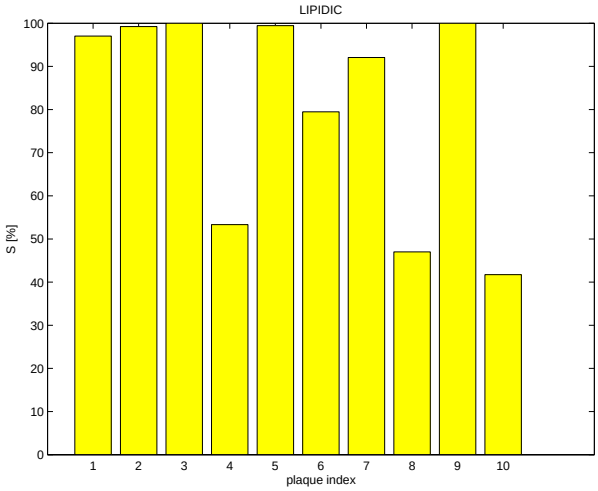

(*b*)

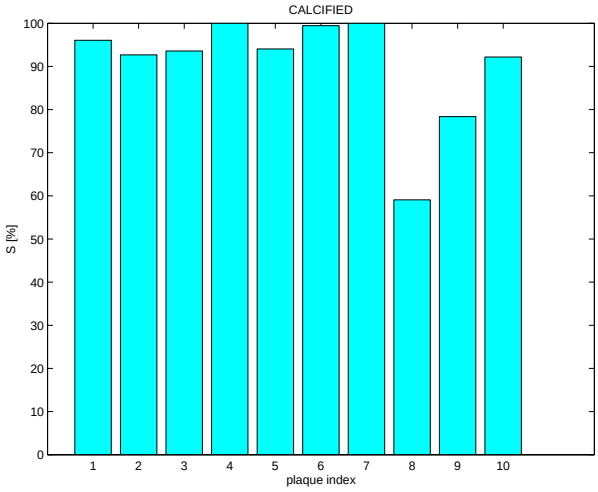

(*c*)

Figure 26: Values of sensitivity for the fibrotic (green), lipidic (yellow) and calcified (cyan) plaque.

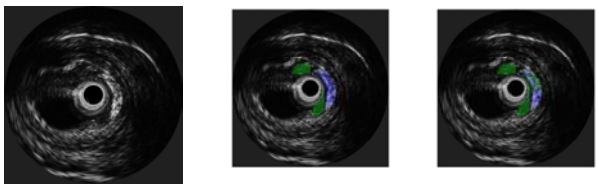

(*a*) (*b*) (*c*)

Figure 27: Example of plaque characterization results. In the column (a) the IVUS image, in (b) the ground truth, segmented according to the histological analysis and in (c) the classification result. In green, yellow and blue are indicated the *fibrotic*, *lipidic* and *calcified* plaque, respectively.

[13] C. Gatta, O. Pujol, O. R. Leor, J. M. Ferre, P. Radeva, Robust image-based ivus pullbacks gating, in: MICCAI '08: Proceedings of the 11th International Conference on Medical Image Computing and Computer-Assisted Intervention, Part II, Springer-Verlag, Berlin, Heidelberg, 2008, pp. 518–525.

[14] S. M. O'Malley, S. G. Carlier, M. Naghavi, I. A. Kakadiaris, Image-based frame gating of IVUS pullbacks: A surrogate for ecg, in: Proc. IEEE International Conference on Acoustics, Speech and Signal Processing ICASSP 2007, Vol. 1, 2007, pp. I–433–I–436. doi:10.1109/ICASSP.2007.366709.

[15] H. Zhu, K. D. Oakeson, M. H. Friedman, Retrieval of cardiac phase from IVUS sequences, in: Medical Imaging 2003: Ultrasonic Imaging and Signal Processing., Vol. 5035, 2003, pp. 135–146.

[16] S. de Winter, R. Hamers, M. Degertekin, K. Tanabe, P. A. Lemos, P. W. Serruys, J. R. Roelandt, N. Bruining, Retrospective image-based gating of intracoronary ultrasound images for improved quantitative analysis: The intelligate method, Catheterization and Cardiovascular Diagnosis 61 (1) (2004) 84–94.

[17] S. O'Malley, M. Naghavi, I. Kakadiaris, Image-based frame gating for contrast-enhanced IVUS sequences, in: Proceedings of Computer Vision for Intravascular and Intracardiac Imaging (CVII), Copenhagen, Denmark, 2006.

[18] J. Barajas, K. L. Caballero, O. Rodriguez, P. Radeva, Cardiac phase extraction in IVUS sequences using 1-D gabor filters, in: 29th Annual International Conference of the IEEE Engineering in Medicine and Biology Society 2007, IEEE, 2007, pp. 343–346.

[19] J. Amores, P. Radeva, Registration and retrieval of highly elastic bodies using contextual information, Pattern Recognition Letters 26 (2005) 1720–1731.

[20] J. Amores, N. Sebe, P. Radeva, Context-based object-class recognition and retrieval by generalized correlograms, Pattern Analysis and Machine Intelligence, IEEE Transactions on 29 (10) (2007) 1818–1833.

[21] M. Rosales, P. Radeva, O. Rodriguez-Leor, D. Gil, Modelling of image-catheter motion for 3-d IVUS, Medical Image Analysis 13 (2009) 91 – 104. doi:DOI: 10.1016/j.media.2008.06.012.

[22] A. Hernandez, P. Radeva, A. Tovar, D. Gil, Vessel structures alignment by spectral analysis of IVUS sequences, in: Proceedings of Computer Vision for Intravascular and Intracardiac Imaging (CVII), Copenhagen, Denmark, 2006.

[23] E. Castro, C. Morandi, Registration of translated and rotated images using finite fourier transforms, IEEE Trans. on PAMI 9 (1987) 700–703.

[24] M. Danilouchkine, F. Mastik, A. van der Steen, Accuracy in prediction of catheter rotation in IVUS with feature-based optical flow – A phantom study, Information Technology in Biomedicine, IEEE Transactions on 12 (3) (2008) 356–365.

[25] C. Gatta, O. Pujol, O. R. Leor, J. M. Ferre, P. Radeva, Fast rigid registration of vascular structures in ivus sequences, IEEE Transactions on Information Technology in Biomedicine accepted. doi:10.1109/TITB.2009.2027230.

[26] G. Loy, A. Zelinsky, A fast radial symmetry transform for detecting points of interest, in: ECCV '02: Proceedings of the 7th European Conference on Computer Vision-Part I, Springer-Verlag, London, UK, 2002, pp. 358–368.

[27] C. Gatta, O. Pujol, O. R. Leor, J. M. Ferre, P. Radeva, Fast rigid registration of vascular structures in ivus sequences, IEEE Transactions on Information Technology in Biomedicine accepted. doi:10.1109/TITB.2009.2027230.

[28] J.D.Klingensmith, D.G.Vince, B.D.Kuban, R.Shekhar, E.M.Tuzcu, S.E.Nissen, J.F.Cornhill, Assessment of coronary compensatory enlargement by three-dimensional intravascular ultrasounds, The International Journal of Cardiac Imaging 16(2) (2000) 87–98.

[29] X.Zhang, C.R.McKay, M.Sonka, Tissue characterization in intravascular ultrasound images, IEEE Transaction on Medical Imaging 17(6) (1998) 889–899.

[30] K.L.Caballero, J.Barajas, O.Pujol, O.Rodriguez, P.Radeva, Using reconstructed ivus images for coronary plaque classification, Proceedings of the 29th Annual International Conference of the IEEE EMBS.

[31] S. K. Mehta, J. R. McCrary, A. D. Frutkin, W. J. Dolla, S. P. Marso, Intravascular ultrasound radiofrequency analysis of coronary atherosclerosis: an emerging technology fot the assessment of vulnerable plaque, European Heart Journal 28 (2007) 12831288.

[32] S. G. Carlier, K. Tanaka, A. Katouzian, Atherosclerotic plaque characterization from radio frequency ultrasound signal processing, US Cardiovascular Disease.

[33] D.Bedekar, Atherosclerotic plaque characterization by acoustic impedance analysis of intravascular ultrasound data, IEEE Ultrasonic Symposium 1527.

[34] W. Tobocman, K. Santosh, J. R. Carter, E. Haacke, Tissue characterization of arteries with 4mhz ultrasound, Ultrasonics 33 (1994) 331–339.

[35] M.Moore, T.Spencer, D.Salter, P.Kearney, T.Shaw, I.Starkey, P.Fitzgerald, R.Erbel, A.Lange, N.McDicken, G.Sutherland, K.Fox, Characterisation of coronary atherosclerotic morphology by spectral analysis of radiofrequency signal: in vitro intravascular ultrasound study with histological and radiological validation, Heart 79(5) (1998) 459467.

[36] Sathyaranayana, Characterization of atherosclerotic plaque by spectral similarity of radiofrequency intravascular ultrasound signals, EuroPCR Online.

[37] A.Katouzian, S.Sathyanarayana, B.Baseri, E.E.Konofagou, S.G.Carlier, Challenges in atherosclerotic plaque characterization with intravascular ultrasound (ivus): from data collection to classification, IEEE Trans Inf Technol Biomed. 12(3): (2008) 315–27.

[38] A.Nair, B.D.Kuban, N.Obuchowski, G.D.Vince, Assessing spectral algorithms to predict atherosclerotic plaque composition with normalized and raw intravascular ultrasound data, Ultrasound in Medicine and Biology 27(10) (2001) 1319–1331.

[39] A.Nair, B.D.Kuban, E.M.Tuzcu, P.Schoenhagen, S.E.Nissen, D.G.Vince, Coronary plaque classification with intravascular ultrasound radiofrequency data analysis, Circulation 106 (2002) 2200–2206.

[40] F. Ciompi, O.Pujol, O. R. Leor, C. Gatta, A. S. Vida, P. Radeva, Enhancing in-vitro ivus data for tissue characterization, Lecture Notes in Computer Science 5524 (2009) 241–248.

[41] M. Kawasaki, H. Takatsu, T. Noda, Y. Ito, A. Kunishima, M. Arai, K. Nishigaki, G. Takemura, N. Morita, S. Minatoguchi, H. Fujiwara, Noninvasive quantitative tissue characterization and two-dimensional color-coded map of human atherosclerotic lesions using ultrasound integrated backscatter, Journal of the American College of Cardiology 38(2) (2001) 486–492.

[42] M. Kawasaki, H. Takatsu, T. Noda, K. Sano, Y. Ito, K. Hayakawa, K. Tsuchiya, M. Arai, K. Nishigaki, G. Takemura, S. Minatoguchi, T. Fujiwara, H. Fujiwara, Invivo quantitative tissue characterization of human coronary arterial plaques by use of integrated backscatter intravascular ultrasound and comparison with angioscopic findings, Circulation 105 (2002) 2487–2492.

[43] M. Kawasaki, K. Sano, M. Okubo, H. Yokoyama, Y. Ito, I. Murata, K. Tsuchiya, S. Minatoguchi, X. Zhou, H. Fujita, H. Fujiwara, Volumetric quantitative analysis of tissue characteristics of coronary plaques after statin therapy using three-dimensional integrated backscatter intravascular ultrasounds, Journal of the American College of Cardiology 45(12).

[44] M. Milunski, G. Mohr, J. Perez, Z. Vered, K. A. Wear, C. J. Gessler, B. E. Sobel, J. Miller, S. A. Wickline, Ultrasonic tissue characterization with integrated backscatter. acute myocardial ischemia, reperfusion, and stunned myocardium in patients, Circulation 80 (1989) 491–503.

[45] A.Murashige, T.Hiro, T.Fujii, K.Imoto, T.Murata, Y.Fukumoto, M.Matsuzaki, Detection of lipid-laden atherosclerotic plaque by wavelet analysis of radiofrequency intravascular ultrasound signals: In vitro validation and preliminary in vivo application, Journal of the American College of Cardiology 45, Issue 12 (2005) 1954–1960.

[46] A.Katouzian, B.Baseri, E.E.Konofagou, A.F.Laine, Automatic detection of blood versus non-blood regions on intravascular ultrasound (ivus) images using wavelet packet signatures, Proc. SPIE, 6920.

[47] P. S. Addison, The Illustrated Wavelet Transform Handbook, 2002.

[48] C. L. de Korte, G. Pasterkamp, A. F. W. van der Steen, H. A. Woutman, N. Bom, Characterization of plaque components with intravascular ultrasound elastography in human femoral and coronary arteries in vitro, Circulation 102 (2000) 617–623.

[49] C. L. de Korte, A. F. W. van der Steen, E. I. Cespedes, G. Pasterkamp, S. G. Carlier, F. Mastik, A. H. Schoneveld, P. W.Serruys, N. Bom, Characterization of plaque components and vulnerability with intravascular ultrasound elastography, Circulation 102 (2000) 617–623.

[50] C. L. de Korte, M. J. Sierevogel, F. Mastik, C. Strijder, J. A. Schaar, E. Velema, G. Pasterkamp, P. Serruys, A. F. van der Steen, Identification of atherosclerotic plaque components with intravascular ultrasound elastography in vivo: a yucatan pig study, Circulation. 105(14) (2002) 1627–30.

[51] J. A. Schaar, E. Regar, F. Mastik, E. P. McFadden, F. Saia, C. Disco, C. L. deKorte, P. J. de Feyter, A. F. van der Steen, P. W. Serruys, Characterizing vulnerable plaque features with intravascular elastography, Circulation 109 (2004) 2716–2719.

[52] A. Van der Steen, C. de Korte, J. Schaar, F. Mastik, R. Baldewsing, P. Serruys, 3d intravascular ultrasounds palpography for vulnerable plaque detection, IEEE International Symposium on Biomedical Imaging: Nano to Macro 1 (2005) 49– 52.

[53] R. L. Maurice, J. Fromageau, M. H. R. Cardinal, M. Doyley, E. de Muinck, J. Robb, G. Cloutier, Characterization of atherosclerotic plaques and mural thrombi with intravascular ultrasound elastography: a potential method evaluated in an aortic rabbit model and a human coronary artery, TITB 12(3).

[54] S. Escalera, O. Pujol, J. Mauri, P. Radeva, Ivus tissue characterization with sub-class error-correcting output codes, Journal of Signal Processing Systems 55 (2008) 35–47.

[55] T.G.Dietterich, G.Bakiri, Solving multiclass learning problems via error-correcting output codes, Journal of Artificial Intelligence Research 2 (1995) 263–286.

[56] R.Rifkin, A.Klautau, In defense of one-vs-all classification, Journal of Machine Learning Research 5 (2004) 101–141.

[57] S. Escalera, O. Pujol, P. Radeva, On the decoding process in ternary error-correcting output codes, IEEE Transactions on Pattern Analysis and Machine Intelligence 99 (1).

[58] K.Tanaka, S.G.Carlier, A.Katouzian, G.S.Mintz, Characterization of the intravascular ultrasound radiofrequency signal within regions of acoustic shadowing behind calcium, JACC 49(9).